PROGRESS REVIEW • OPEN ACCESS

Measuring sliding friction at the atomic scale

OPEN ACCESS

Japanese Journal of Applied Physics **61**, SL0801 (2022) **PROGRESS REVIEW**

https://doi.org/**10.35848/1347-4065/ac5e4a**

Measuring sliding friction at the atomic scale

Alfred J. Weymouth*, Oliver Gretz, Elisabeth Riegel, and Franz J. Giessibl

Institute of Experimental and Applied Physics, University of Regensburg, Universitaetsstrasse 31, 93053 Regensburg, Germany

*E-mail: jay.weymouth@ur.de

Received January 11, 2022; revised February 25, 2022; accepted March 16, 2022; published online June 14, 2022

Sliding friction is a nonconservative force in which kinetic energy is dissipated via various phenomena. We used lateral force microscopy to measure the energy loss as a tip oscillates laterally above a surface with sub-Angstrom amplitudes. By terminating the tip with a single molecule, we ensure the tip ends in a single atom. We have reported that energy is dissipated as a CO molecule at the tip apex is oscillated over pairs of atoms. This is a result of the CO being bent in different directions as the tip moves in one direction and then in the other. We confirm this with a model that describes the CO on the tip as a torsional spring. Surprisingly, we only observe dissipation within a small range of tip heights. This allows us to determine the necessary components to model friction and shows how sensitive friction is to the local potential energy landscape.

1. Introduction

When macroscopic surfaces slide against each other, the frictional properties are determined by micro- or mesoscopic asperities. The roughness of the surface defines the size and shape of these individual asperities, as sketched in Fig. 1(a). Sliding friction is a complex phenomenon that describes kinetic energy being dissipated into other forms. This can involve the breaking of chemical bonds, the creation of photons (triboluminescence) and the creation of phonons.

Because friction in macroscopic objects is determined by small asperities, it is natural that friction has been studied extensively with friction force microscopy (FFM).[1,2] FFM is a derivative of atomic force microscopy in which the tip is pressed against the surface and the lateral force is measured. With a sharp FFM tip, this technique can probe friction with a single asperity, as sketched in Fig. 1(b).[3] In a typical optical setup where a laser is reflected off the back of the cantilever, the twisting of the cantilever (its deflection) is measured and via knowledge of the torsional spring constant, the lateral forces can be directly determined. By integrating the lateral forces over a closed path, for instance as the cantilever first sweeps over the sample in one direction and then the other, the energy dissipation can be calculated.

Whereas we are all familiar with the concept of friction that involves wear, in which material is lost from the sliding surfaces (and the reason that we need to replace the brake pads in our bicycles or automobiles), wearless friction is also a major component that leads to energy dissipation. Almost 100 years ago, two models were independently proposed to understand wearless friction, first by Prandtl[4] and a year later by Tomlinson.[5] If we consider the interaction of a single particle on one surface sliding over the other surface, where the single particle is attached to the respective bulk by a spring-like potential, then during sliding the spring can first be loaded as the particle is trapped behind a potential energy barrier and then quickly releases as it snaps over.

This stick-slip motion at the atomic level does not require a single particle to be slid over a surface, and it has been detected with FFM. Atomic friction was first reported by Mate and coworkers who recorded lateral forces (frictional forces) of a tungsten tip sliding over a graphite surface.[6]

We have worked on a technique which allows us to probe lateral forces acting on a sliding surface that ends in a single atom, as shown in Fig. 1(c). To do this, we start with a technique able to measure forces with atomic spatial resolution, frequency-modulation atomic force microscopy (FM-AFM).[7] In it, the tip is mounted on a cantilever and driven to oscillate at its resonance frequency with a sinusoidal drive signal. Conservative force interaction with the surface changes the frequency of oscillation and dissipative force interaction requires an increase in the drive signal, both of which are measured simultaneously. We want to measure lateral forces, and therefore we construct a sensor whose first flexural mode results in the tip oscillating laterally over the surface. In this sense, a self-sensing sensor like the qPlus AFM sensor[8] is an excellent starting point, as we do not need to re-align a laser reflecting off the cantilever. Sensor modifications were first presented in Ref. 9 and later in Ref. 10. We call this technique lateral force microscopy (LFM),[11] to distinguish it from FFM.

As LFM is a scanning probe technique capable of atomic resolution which can be operated in the non-contact regime, we can use tip engineering techniques to control the apex of the tip down to one single atom. Defining and understanding one of the sliding surfaces down to the single atom is a very powerful component of this technique. Another important attribute of the qPlus-based sensor is that its high stiffness allows us to control the oscillation with amplitudes less than 100 pm. As the oscillation is lateral, in order to investigate single atomic phenomena, we need to oscillate with an amplitude that is less than half of the distance between atoms. For atomic resolution, amplitudes less than interatomic distances are required.

At this point, it is important to note that FFM (implemented such that many atoms of the tip slide across the surface) and LFM (implemented such that one or a few atoms are involved in sliding friction) are both powerful tools but are best used for different investigations. For ensemble phenomena such as superlubricity, which involves a stiff

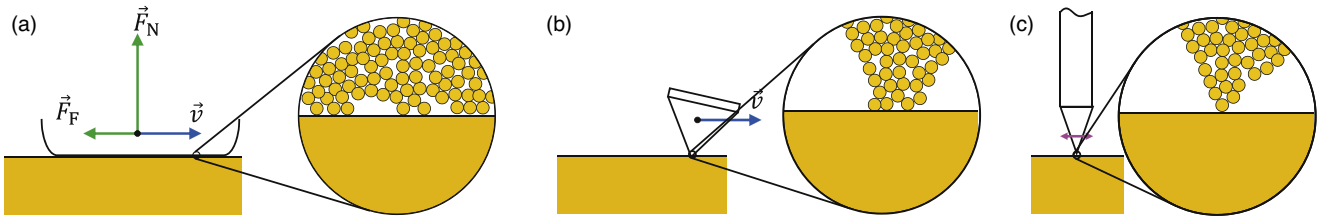

Fig. 1. (Color online) At different length scales, friction can be dominated by different structures. (a) Macroscopic sliding friction is dominated by several asperities, sketched in the zoom-in. (b) Smaller sliding surfaces, such as those found in FFM, can measure with a single asperity. (c) With LFM, a single atom asperity can be generated.

lattice that cannot "lock" into the potential energy landscape of the surface,[12] such as a flake of graphene,[13] FFM is required. FFM has also been used to investigate the effect of local doping in a silicon probe[14] and to probe the effects of various isotopes on friction.[15] When we want to investigate the influence of phenomena at the length scale of single atoms[16] including dangling bonds, LFM is required. LFM also can be performed such that there is no wear or damage to the atomic asperity.

2. Lateral force microscopy (LFM)

The following experiments discussed in this review article were all performed with microscopes operating in ultra-high vacuum cooled with liquid helium ($T \approx 5$ K).

One advantage of LFM that does not relate directly to friction is that it can detect forces and potential energy with the tip at a precise height over the surface. While sub-Angstrom amplitudes used might seem very small, they are significant compared to the length scales of atomic interactions. For example, if one oscillates with 50 pm (a typical value for normal-force FM-AFM in current literature), then the peak to peak swing is 100 pm. There are systems that change quite drastically over distances of 100 pm. One example is a single copper phthalocyanine molecule on the Cu(111) surface.[17] Nominally, this molecule sits with one of its four lobes aligned to a high-symmetry direction of the underlying copper atoms. When the tip approaches, however, the molecule jumps to a rotated state. We studied this system with LFM, where the tip is nominally at the same height above the molecule. With it, we were able to understand the change in the potential energy of the tip-molecule interaction and how that affected the potential energy landscape.

Similar to FM-AFM where the normal force is measured, the amplitude of the oscillation is measured and controlled by the control electronics by appropriately changing the drive signal. A measure of the conservative force interaction is the frequency shift, Δf. When there is an increase in dissipation, we observe an increase in the drive signal. The change in the drive signal can be converted into the energy loss per oscillation cycle, E_{diss}.[18]

A unique challenge of an LFM sensor is the determination of the stiffness k. The calculation of forces, energies and dissipative energies require the knowledge of k.[18,19] For conventional AFM (i.e. measurements of the normal force) with a sufficiently small tip attached perpendicular to the end of the prong, k does not change significantly from the stiffness of the bare prong.[20–22] This is because the tip is vertically very stiff and therefore applied forces are transferred directly—with a minimum of mechanical deformation—to the cantilever. In case of LFM, where forces act perpendicular on the tip, bending of the tip can occur. Even if the tip was infinitely stiff, it would increase the effective length of the tine, and thus decrease the stiffness k. In the appendix we present an application of the Euler–Bernoulli beam theory including a softer tip to more accurately calculate the LFM sensor stiffness.

3. Understanding the atomic system

Our implementation of LFM is with the stiff qPlus sensor.[8,9] This allows us to take advantage of the tip engineering techniques that have been pioneered in the STM and AFM communities. These techniques are typically performed on a metal surface at low temperature (liquid helium) in ultra-high vacuum with the help of a small dose of CO molecules. CO is a well-studied small molecule whose adsorption geometry is well-known. In one configuration, we use it as a probe of the tip, so that we can identify the number and position of the apex atoms.[23–26] In the opposite configuration, we pick up the CO from the surface such that it is bound to the tip apex.

Using STM, Bartels et al. first determined that a single CO molecule could be picked up at the apex of a metal tip.[27] Later, Gross et al. showed that the CO can play an important role in improving the spatial resolution of FM-AFM images: At the tip, the CO molecule reduces the chemical reactivity, allowing adsorbates to be probed in the region where Pauli repulsion dominates between the tip and sample.[28,29] This has made it a very important tip termination for the FM-AFM community, as it is straightforward to prepare and allows for submolecular resolution of flat organic molecules. This exciting ability has led to the CO tip being the focus of several studies.[30–32]

One attribute of the CO tip, apart from it being chemically inert, is that it bends in response to lateral forces.[28,30] This can be seen in the AFM images of flat organic molecules in which the atomic positions appear to be slightly shifted from their actual positions.[33] Understanding how the CO molecule responds to lateral forces, however, is challenging for theoretical calculations to predict. Determining this was therefore an excellent application of LFM as it is a natural technique to measure the applied lateral forces.

As discussed in Ref. 34, we collected data of a CO tip scanning above a single CO molecule on the Cu(111) surface. We acquired constant-height images as close as we could until the CO laterally displaced. We then converted the acquired Δf signal and determined the lateral force as a function of both vertical and lateral distances. This followed a typical pattern of attraction and then repulsion as the distance decreased, as one would expect from an empirical Lennard-

Jones or Morse potential. The question we then posed was how accurately do these empirical potentials describe the system?

We used a Morse potential as a function of the distance between the two oxygen atoms to describe the tip-sample interaction. We also allowed the CO at the tip and the CO on the sample to relax as torsional springs with different spring constants, as sketched in Fig. 2. The calculated LFM signal provided excellent agreement to our data. From this, we concluded (1) that empirical potentials can be an excellent description of interatomic interaction, especially with a CO tip; and (2) that the CO tip does behave like a torsional spring.

Interestingly, in this experiment, we did not observe dissipation. The forces acting upon the tip were nominally the same in both directions. Even in the case where the tip was on average directly above the surface CO molecule, both CO molecules had enough degrees of freedom that they could slide around each other without producing measurable dissipation.

4. Observing sliding friction

One possibility to measure dissipation during sliding friction involves the CO molecule being locked between two atoms. In essence, this removes one degree of freedom compared to the CO at the tip sliding over a CO on the surface. We collected data of the more complex system of PTCDA on Cu (111), as first presented in Ref. 35. When PTCDA molecules are evaporated on the surface at room temperature at submonolayer coverage, they lie flat on the surface and form islands. Figure 3 shows the STM, Δf and E_{diss} measurements that were simultaneously acquired.

In the STM channel, the individual molecules can be easily made out as they also contain intramolecular contrast. The contrast (like previously reported AFM images) shows features similar to the ball-and-stick figures of the molecules themselves. The contrast is not overall uniform, which we believe is because the molecules do not lie flat on the surface.

The LFM Δf image has very strong features that depend strongly on the oscillation direction of the tip relative to the nearby atoms. If we consider features between two atoms that have a chemical bond between them, then it can be observed that the bonds that lie perpendicular to the oscillation direction are much stronger in signal than those that lie parallel. At this height, the molecules appear slightly distorted. This is because at this height there is substantial interaction with the tip.

Finally, the E_{diss} image shows very sharp features. All of these features correspond to the strong lines in the LFM image (although the reciprocal is not true). These are very strong and local features that can predominantly be seen over chemical bonds.

The LFM and the E_{diss} data can be understood via two complementary models: A modified probe-particle model (PPM)[17,36] and a strumming model.[35] The modified PPM can only be used to consider conservative force interaction, whereas the current implementation of the strumming model is limited to one high-symmetry direction. As this review article concerns energy dissipation, we focus on the strumming model.

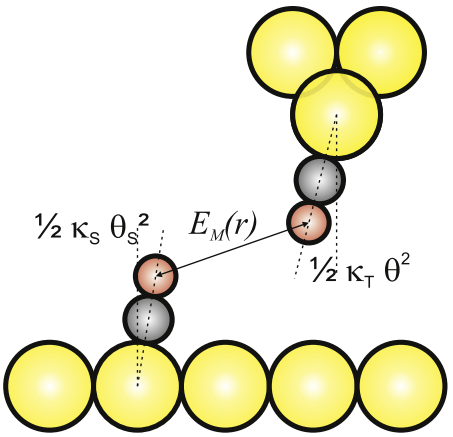

Fig. 2. (Color online) For the CO-CO system, the total energy is described by (1) a term describing the torsional spring of the surface CO, (2) a similar term for the CO at the tip, and (3) a Morse potential considering the distance between the oxygen atoms.

The strumming model needs to explain energy dissipation during the oscillation of the tip. We did not observe energy dissipation in the case of CO-CO interaction because the CO at the tip was able to slide "around" the CO on the surface. Therefore the CO on the tip must be trapped between two surface atoms in order to observe this phenomenon. To simplify calculations, we confine the tip to a high-symmetry direction between the two atoms and calculate the potential energy of the system as the sum of the Morse potentials between surface atoms and apex O atom, and the torsional spring as a function of its deflection angle. The surface atoms are not allowed to relax.

In Fig. 4(a), the total energy as a function of the bending angle is plotted for various lateral distances to the chemical bond. The positions relative to the chemical bond, located at $x = 0$ pm, are shown in Fig. 4(b). At certain positions there are two local low-energy solutions, as can be seen in Fig. 4(a) iii, iv and v. However, the tip CO molecule does not necessarily find the thermodynamic minimum solution at all times. That is, it can be kinetically trapped in a local low-energy solution with an energy barrier between it and the global energy minimum. In order for the CO to move from a local low-energy solution to the global low-energy solution, the energy barrier must be small enough. We assumed this means that the energy barrier is less than k_BT, where $T = 5.5$ K is the temperature and k_B is Boltzmann's constant.

We can now consider what happens when the tips is above a chemical bond and oscillates. As the CO approaches, the CO molecule is attracted to the atoms and it bends towards the bond. As it continues to get closer, Pauli repulsion causes it to be pushed back. The angle decreases and more energy is stored in the torsional spring as the tip moves across the chemical bond. This can be seen, for example, as the angle continues to decrease in Fig. 4(b) between points ii to iv. Finally from points iv to v in Figs. 4(b) and 4(c), the CO swings over the chemical bond.

The forward motion [blue solid lines in Figs. 4(b) and 4(c)] is different from the backward motion [red dashed line in Figs. 4(b) and 4(c)], meaning that the path of the apex O atom of the tip is different. The forces acting upon the tip are different, as can be seen in Fig. 4(c).

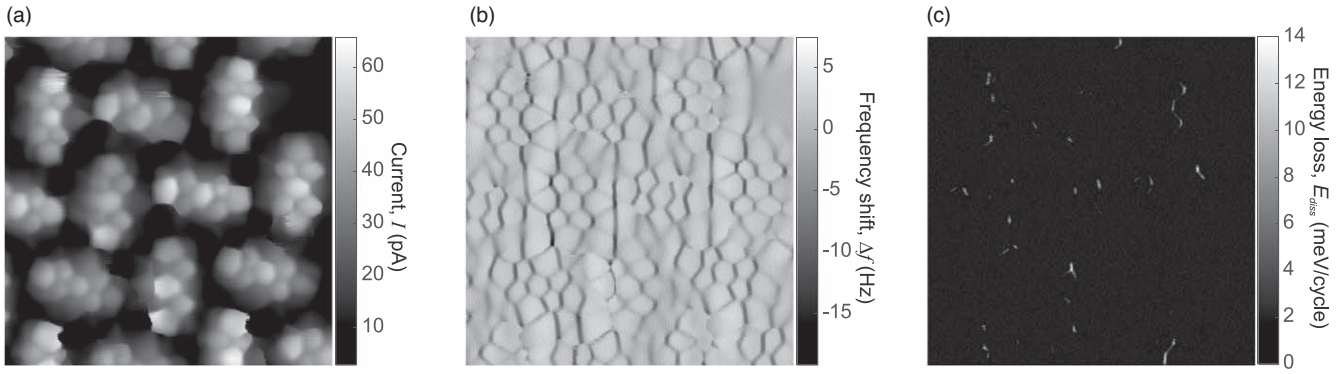

Fig. 3. An island of PTCDA molecules on Cu(111) collected at constant height with a voltage of 1 mV. Image size is 4 nm × 4 nm. The tip is oscillated horizontally (left-right direction) with an amplitude of 20 pm. (a) STM (b) frequency shift LFM (c) energy dissipation.

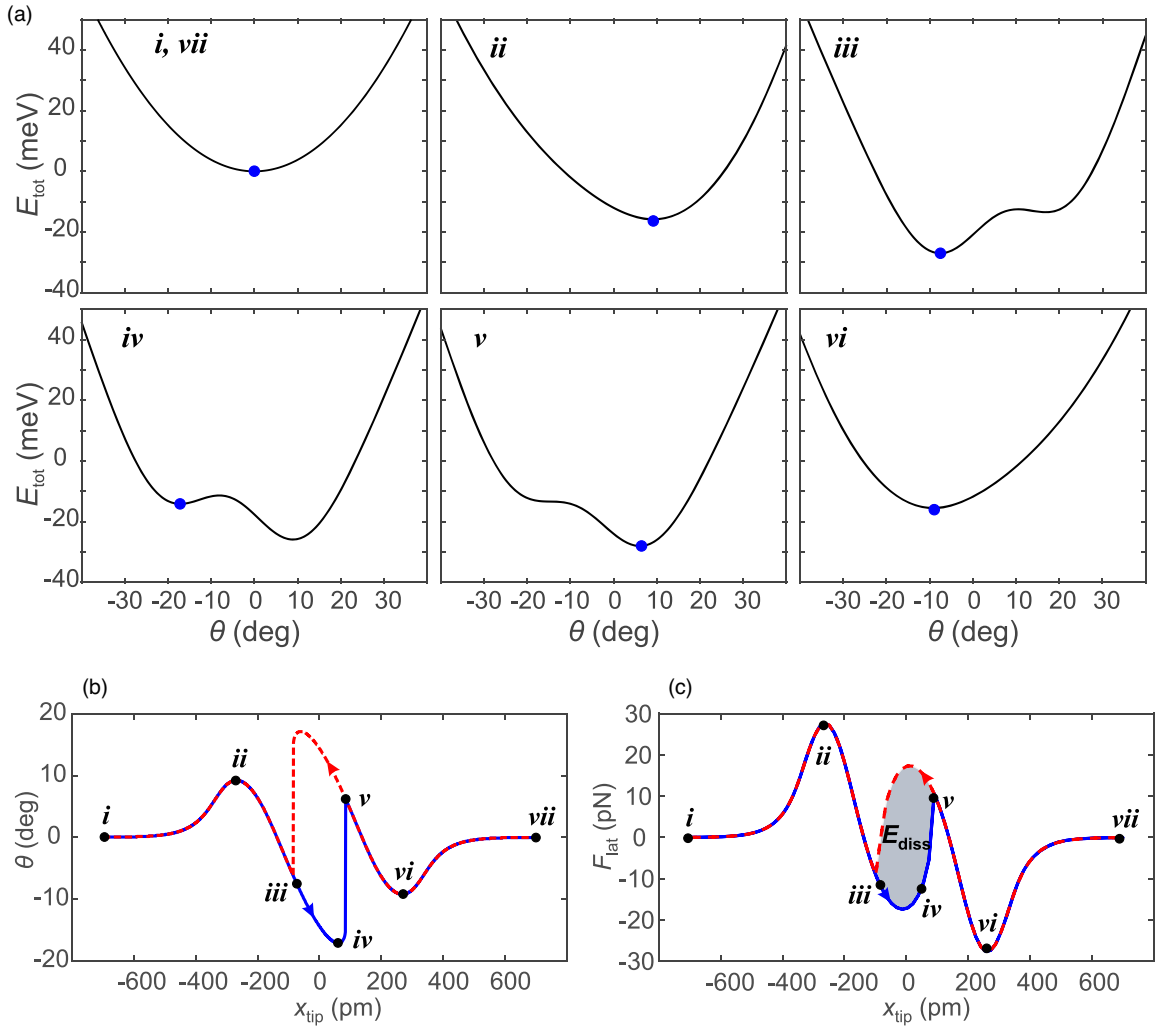

Fig. 4. (Color online) At each point, the potential energy E_{tot} is calculated as a function of the deflection angle of the CO at the tip apex. The apex metal atom is located at x_{tip}, where 0 pm corresponds to directly above the chemical bond. In b and c, the blue line refers to motion in the $+x$ direction, and the red dotted line refers to motion in the $-x$ direction.

In order for there to be energy dissipation, different lateral forces must act on the tip in the forward and backward stages of the oscillation cycle. In order for us to be sensitive to this energy dissipation, it must occur with each oscillation cycle. This oscillation happens many times for each pixel: The scan speed of the AFM is rather slow (sub-Hertz) compared to the oscillation frequency (tens of kilohertz).

When the tip does not oscillate above the chemical bond, the lateral forces acting on the tip forward and backward are the same, so the work done on the tip (integral of the lateral force acting on the tip over one oscillation cycle) is zero. In other words, there is only conservative force interaction and we do not observe energy dissipation. This is also true when the tip is too high above a chemical bond, and Pauli repulsion does not result in the torsional spring of the CO to be loaded and then released.

Conversely, if the tip is too low, then the CO only snaps over once and not in every oscillation cycle. We included this

in the model that we published in Ref. 35, in that two oscillation cycles are simulated. If the snap takes place in the first and the second, we can assume that it will occur in each oscillation cycle.

Dissipation will only be measured if the tip motion encloses the hysteresis loop shown in gray in Fig. 4(c). In the case where only two surface atoms are simulated, the hysteresis loop is relatively wide. Including more atoms reduces its width, which shows clearly how the total potential energy landscape is strongly influenced not only by the atoms that directly interact with the tip via Pauli repulsion, but also nearby atoms as well.

5. Outlook

One of the most exciting aspects of these measurements is that they are truly unique to LFM. FM-AFM measurements, in which the tip oscillates vertically, do not measure energy dissipation for this lateral snapping.

Currently our model does not explicitly include a mechanism of energy dissipation. It would nominally be the CO molecule swinging after snapping and slowly decreasing in oscillation. This would most likely involve energy transfer in the form of phonons to the tip apex.

In order to better understand the energy dissipation and the complex potential energy landscape, we are working with Oliver Hofmann from TU Graz who is using DFT-based techniques to simulate this system.

Experimentally, we are also looking to incorporate normal force measurements in our setup. We have recently demonstrated that both LFM and AFM are possible with a qPlus sensor by using the length-extension and first flexural modes at room temperature.[37] Yamada et al. have also proposed implementing simultaneous LFM measurements with a longer tip that will oscillate laterally at the second flexural mode.[38]

LFM is an exciting technique that is relatively straightforward to implement in any existing qPlus-based system. It allows investigation at the natural spatial limit of single atoms. With LFM, we look forward to more exciting discoveries as we probe the ubiquitous phenomenon of sliding friction.

Acknowledgments

The first author would like to thank Takashi Ichii and the organizers of the 29th International Colloquium on Scanning Probe Microscopy for their kind invitation to present this work. We would also like to thank N. Okabayashi for his feedback on this work, inspiring Fig. 4. A.J.W. and O.G. thank the German Research Foundation ("Locally mapping conductance and potential energy of a donor-acceptor system", project number 397 771 090) for funding.

Appendix A.

A.1 LFM sensor stiffness calculation

Figure A·1 shows a simplified LFM sensor as a rectangular cantilever and a cylindrical tip at the end, ignoring the glue and the conical ending of the tip. We begin with the static bending equation for a point-like force F applied at $x = L$:[39]

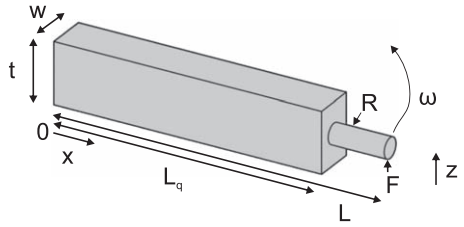

Fig. A·1. LFM sensor parameterization: w is the thickness of the cantilever, t the width, L_q the length. L is the length including the cantilever and the tip, R is the radius of the tip, and F the applied force at the end of the tip. ω represents the total deflection of the combined beam.

$$\frac{d^2\omega}{dx^2} = \frac{F(L-x)}{E(x)I(x)}, \tag{A·1}$$

where $I(x)$ is the second moment of area and the $E(x)$ is the Young's modulus. ω is the deflection in the z direction (see Fig. A·1). For a rectangular cross-section of the cantilever and a circular cross-section of the tip, $I(x)$ can be written as:[39]

$$I(x) = \begin{cases} I_q = \dfrac{1}{12}wt^3, & 0 \leqslant x \leqslant L_q \\ I_t = \dfrac{1}{4}\pi R^4, & L_q < x \leqslant L \end{cases} \tag{A·2}$$

w, t, and R are defined in Fig. A·1.

The Young's modulus $E(x)$ is also piecewise defined considering the different materials of the cantilever and the tip:

$$E(x) = \begin{cases} E_q, & 0 \leqslant x \leqslant L_q \\ E_t, & L_q < x \leqslant L. \end{cases} \tag{A·3}$$

E_q is the Young's modulus of the cantilever (quartz) and E_t of the tip (tungsten).

The first derivative of ω can be calculated by integrating Eq. (A·1):

$$\frac{d\omega(x)}{dx} = \begin{cases} \displaystyle\int_0^x \frac{F(L-l)}{E_q I_q}dl, & 0 \leqslant x \leqslant L_q \\ \displaystyle\int_0^{L_q} \frac{F(L-l)}{E_q I_q}dl + \int_{L_q}^x \frac{F(L-l)}{E_t I_t}dl, & L_q < x \leqslant L. \end{cases} \tag{A·4}$$

$$= \begin{cases} \dfrac{F}{E_q I_q}(Lx - \dfrac{1}{2}x^2), \\ \dfrac{F}{E_q I_q}(LL_q - \dfrac{1}{2}L_q^2) + \dfrac{F}{E_t I_t}(Lx - \dfrac{1}{2}x^2 - LL_q + \dfrac{1}{2}L_q^2) + C_1 \end{cases}, \tag{A·5}$$

where C_1 is an integration constant. The values for x of Eq. (A·4) are also valid for Eq. (A·5). C_1 has to be determined to fullfil the continuity conditions:

$$\left.\frac{d\omega}{dx}\right|_{x=0} = 0 \tag{A·6}$$

$$\left.\frac{d\omega}{dx}\right|_{x=L_q}, \text{ continuous.} \tag{A·7}$$

Equation (A·6) is fulfilled. Condition (A·7) leads to

$$C_1 = 0 \tag{A·8}$$

$\omega(x)$ can be calculated by integrating Eq. (A·5) one more time:

$$\omega(x) = \begin{cases} \int_0^x \frac{F}{E_q I_q}(Ll - \frac{1}{2}l^2)dl, & 0 \leqslant x \leqslant L_q \\ \int_{L_q}^x \left(\frac{F}{E_q I_q}(LL_q - \frac{1}{2}L_q^2)\right)dl & \\ +\int_{L_q}^x \left(\frac{F}{E_t I_t}(Ll - \frac{1}{2}l^2 - LL_q + \frac{1}{2}L_q^2)\right)dl, & L_q < x \leqslant L \end{cases} \tag{A·9}$$

$$= \begin{cases} \frac{F}{E_q I_q}\left(\frac{1}{2}Lx^2 - \frac{1}{6}x^3\right), & 0 \leqslant x \leqslant L_q \\ F\left(\frac{1}{E_q I_q} - \frac{1}{E_t I_t}\right)\left(LL_q - \frac{1}{2}L_q^2\right)(x - L_q) & \\ +\frac{F}{E_t I_t}\left(\frac{1}{2}Lx^2 - \frac{1}{6}x^3 - \frac{1}{2}LL_q^2 + \frac{1}{6}L_q^3\right) + C_2, & L_q < x \leqslant L \end{cases} \tag{A·10}$$

Since $\omega(x)$ has to be continous at $x = L_q$ the integration constant can be determined to be:

$$C_2 = \frac{F}{E_q I_q}\left(\frac{1}{2}LL_q^2 - \frac{1}{6}L_q^3\right). \tag{A·11}$$

Using Hook's law the stiffness can be calculated by

$$k = \frac{F}{\omega(L)}. \tag{A·12}$$

A.2 Stiffness calculation with real values

Table A·1 shows the values for the stiffness calculation of a typical LFM sensor. With these values a stiffness of $k = 1343$ N m^{-1} was obtained. Figure A·2 shows the plot of $\omega(x)$ from 0 to L.

A.3 Static bending measurements

To validate the Euler–Bernoulli theory calculations presented in the section above, static bending measurements on a S1.0 Statek qPlus sensor with a tip in LFM configuration were performed. The tip was a tungsten wire with diameter 125 μm and length 2.0 mm.

Figure A·3 shows the setup of the experiment. A qPlus sensor with a tip was glued on an aluminum block and a weight was attached at different positions dL at the tip. This led to a bending dz of the prong and the tip, which was measured with an optical microscope (Keyence VHX-600 from Keyence Deutschland GmbH, Germany). The stiffness k was then calculated by $k = \frac{F}{dz} = \frac{mg}{dz}$, where $g = 9.81$ m/s/s. A small screw with weight $m = 0.500$ g was used as the mass, which was hung on the tip with a small gold wire with diameter 25 μm. The additional mass of the gold wire was not measurable with the precision scale Sartorius Basic (Sartorius AG, Germany) (precision 1 μg). The gold wire loop around the mass was closed by gluing the ends together.

Figure A·4 shows the measured stiffness for different positions of the weight on the tip (blue dots). For these positions the theoretical value was calculated with Eqs. (A·10) and (A·12) shown by the orange dots, which considers a circular tungsten tip attached to the cantilever. The position of the mass in the experiment was considered as the tip length in the calculation. The absolute error of the optical microscope was estimated to be 1 μm. At small dL the bending was only 6.48 μm which leads to a relative error of 15.4%. For larger dL the relative error is smaller. The calculated values are in good agreement with the experimental ones for $dL > 1.200$ mm. In most cases the calculated values are within the error bars. Only for small $dL < 0.8$ mm do they lie outside of the error bars. One reason is the limited accuracy of the optical microscope to measure such small bendings. Another is an overestimation of k by the Euler–Bernoulli theory. In the calculation the end of the cantilever is considered to be fixed. This is not the case in a qPlus sensor where deformation of the quartz happens already before the base of the prong.[40] Also the connection of the tip and the cantilever is considered to be infinitely stiff in the

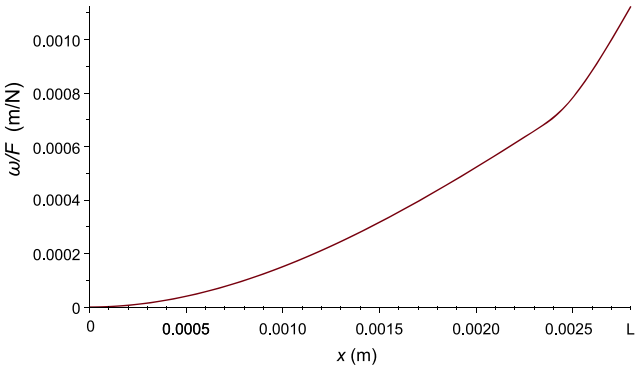

Fig. A·2. (Color online) Plot of $\omega(x)$ from 0 to L.

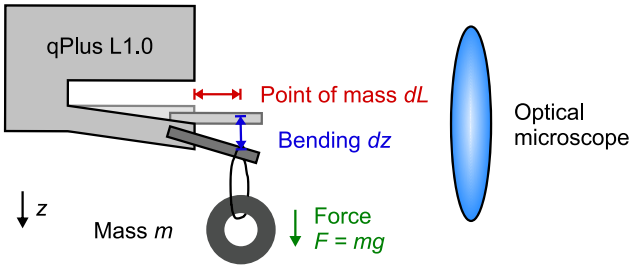

Fig. A·3. (Color online) Static bending experiment. A mass m was attached at different positions on the tip at position dL. This led to the deflection dz which was measured by an optical microscope.

Table A·1. LFM sensor parameters.

Parameter	Value
L	2.33 mm (440 μm tip length)
R	25.0 μm
t	0.214 mm
w	0.127 mm
L_q	1.89 mm
E_q	78.7 GPa
I_q	1.0372e-16 m^4
E_T	400 GPa
I_T	3.0680e-19 m^4
k	1343 N m^{-1}

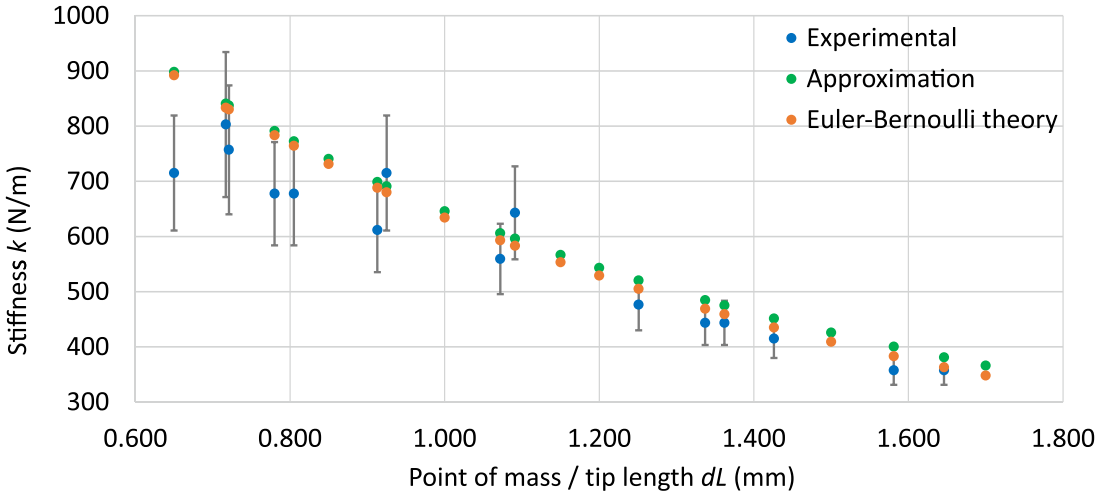

Fig. A·4. (Color online) Blue dots show measured stiffness for various tip length or points of mass. Orange dots are calculated stiffness values with the Euler–Bernoulli theory considering a circular tungsten tip. The green dots are the calculated stiffness using the approximation $k = k_q \frac{L_q^3}{(L_q+\Delta L)^3}$, where k_q is the stiffness of the prong without a tip and ΔL is the length of the tip.

model, which is not the case in a real configuration due to the gluing of the tip.

Another way to approximate the stiffness of a sensor with a tip is by the formula

$$k = k_q \frac{L_q^3}{(L_q + \Delta L)^3.} \tag{A·13}$$

where k_q is the stiffness of the cantilever without a tip and ΔL is the length of the tip.[18] This approximation assumes a tip with the same cross section and the same material as the cantilever. The values calculated with Eq. (A·13) are shown in Fig. A·4 by the green dots. All values lie above the values calculated with Euler–Bernoulli theory. The difference of the approximation to the Euler–Bernoulli calculation increases as function of dL.

In this experiment a tungsten tip with diameter 125 μm was used because a higher weight could be attached on the tip without an irreversible plastic deformation of the tip. For a typical LFM sensors a tip with 50 μm diameter is usually used. The approximation formula considers a "tip" made of quartz with the cross section of the cantilever. Therefore, a higher difference between the stiffness calculated with the Euler–Bernoulli and the approximation formula is expected when a tip with a diameter of 50 μm is used.

In summary the Euler–Bernoulli theory calculation, which considers the extent of a rectangular cantilever with a circular tungsten tip, is a good estimate of the total stiffness of a LFM sensor and superior to the approximation formula for thin tips. Increased accuracy of the static bending experiment, especially for short tip lengths, could be achieved by using an interferometer.

Appendix B.

*

ORCID iDs

Alfred J. Weymouth https://orcid.org/0000-0001-8793-9368
Oliver Gretz https://orcid.org/0000-0002-1046-172X
Franz J. Giessibl https://orcid.org/0000-0002-5585-1326

1) A. Socoliuc, R. Bennewitz, E. Gnecco, and E. Meyer, Phys. Rev. Lett. **92**, 134301 (2004).
2) Q. Li, Y. Dong, D. Perez, A. Martini, and R. W. Carpick, Phys. Rev. Lett. **106**, 126101 (2011).
3) I. Szlufarska, M. Chandross, and R. W. Carpick, J. Phys. D **41**, 123001 (2008).
4) L. Prandtl, Z. Angew. Math. Mech. **8**, 85 (1928).
5) G. Tomlinson, London, Edinburgh, Dublin Philos. Mag. J. Sci. **7**, 905 (1929).
6) C. Mate, G. McClelland, R. Erlandsson, and S. Chiang, Phys. Rev. Lett. **59**, 1942 (1987).
7) T. R. Albrecht, P. Grütter, D. Horne, and D. Rugar, J. Appl. Phys. **69**, 668 (1991).
8) F. J. Giessibl, Appl. Phys. Lett. **73**, 3956 (1998).
9) F. J. Giessibl, M. Herz, and J. Mannhart, Proc. Natl. Acad. Sci. **99**, 12006 (2002).
10) O. Gretz, A. J. Weymouth, T. Holzmann, K. Pürckhauer, and F. J. Giessibl, Beilstein J. Nanotechnol. **12**, 517 (2021).
11) A. J. Weymouth, J. Phys.: Condens. Matter **29**, 323001 (2017).
12) O. Hod, E. Meyer, Q. Zheng, and M. Urbakh, Nature **563**, 485 (2018).
13) M. Dienwiebel, G. Verhoeven, N. Pradeep, J. Frenken, J. Heimberg, and H. Zandbergen, Phys. Rev. Lett. **92**, 126101 (2004).
14) J. Y. Park, D. F. Ogletree, P. A. Thiel, and M. Salmeron, Science **313**, 186 (2006).
15) R. J. Cannara, M. J. Brukman, K. Cimatu, A. V. Sumant, S. Baldelli, and R. W. Carpick, Science **318**, 780 (2007).
16) A. J. Weymouth, D. Meuer, P. Mutombo, T. Wutscher, M. Ondracek, P. Jelinek, and F. J. Giessibl, Phys. Rev. Lett. **111**, 126103 (2013).
17) A. Weymouth, E. Riegel, B. Simmet, O. Gretz, and F. Giessibl, ACS Nano **15**, 3264–71 (2021).
18) F. J. Giessibl, Rev. Mod. Phys. **75**, 949 (2003).
19) A. J. Weymouth, E. Riegel, S. Matencio, and F. J. Giessibl, Appl. Phys. Lett. **112**, 181601 (2018).
20) J. Berger, M. Švec, M. Müller, M. Ledinský, A. Fejfar, P. Jelínek, and Z. Majzik, Beilstein J. Nanotechnol. **4**, 1 (2013).
21) J. Falter, M. Stiefermann, G. Langewisch, P. Schurig, H. Hölscher, H. Fuchs, and A. Schirmeisen, Beilstein J. Nanotechnol. **5**, 507 (2014).
22) J. Melcher, J. Stirling, and G. A. Shaw, Beilstein J. Nanotechnol. **6**, 1733 (2015).
23) J. Welker and F. J. Giessibl, Science **336**, 444 (2012).
24) M. Emmrich et al., Science **348**, 308 (2015).
25) A. Liebig, A. Peronio, D. Meuer, A. J. Weymouth, and F. J. Giessibl, New J. Phys. **22**, 063040 (2020).
26) O. Gretz, A. J. Weymouth, and F. J. Giessibl, Phys. Rev. Res. **2**, 33094 (2020).
27) L. Bartels, G. Meyer, and K.-H. Rieder, Appl. Phys. Lett. **71**, 213 (1997).
28) L. Gross, F. Mohn, N. Moll, P. Liljeroth, and G. Meyer, Science **325**, 1110 (2009).
29) N. Moll, L. Gross, F. Mohn, A. Curioni, and G. Meyer, New J. Phys. **12**, 125020 (2010).

30) Z. Sun, M. P. Boneschanscher, I. Swart, D. Vanmaekelbergh, and P. Liljeroth, Phys. Rev. Lett. **106**, 046104 (2011).
31) M. Ellner, N. Pavliček, P. Pou, B. Schuler, N. Moll, G. Meyer, L. Gross, R. Peréz, and R. Perez, Nano Lett. **16**, 1974 (2016).
32) M. P. Boneschanscher, J. van der Lit, Z. Sun, I. Swart, P. Liljeroth, and D. Vanmaekelbergh, ACS Nano **6**, 10216 (2012).
33) M. Neu, N. Moll, L. Gross, G. Meyer, F. J. Giessibl, and J. Repp, Phys. Rev. B **89**, 205407 (2014).
34) A. J. Weymouth, T. Hofmann, and F. J. Giessibl, Science **343**, 1120 (2014).
35) A. J. Weymouth, E. Riegel, O. Gretz, and F. J. Giessibl, Phys. Rev. Lett. **124**, 196101 (2020).
36) P. Hapala, G. Kichin, C. Wagner, F. S. Tautz, R. Temirov, and P. Jelínek, Phys. Rev. B **90**, 085421 (2014).
37) D. Kirpal, J. Qiu, K. Pürckhauer, A. J. Weymouth, M. Metz, and F. J. Giessibl, Rev. Sci. Instrum. **92**, 043703 (2021).
38) Y. Yamada, T. Ichii, T. Utsunomiya, and H. Sugimura, Jpn. J. Appl. Phys. **58**, 095003 (2019).
39) J. M. Gere and S. P. Timoshenko, *Mechanics of Materials* (Brooks/Cole, Salt Lake City, UT, 1997) 4th ed.
40) A.-K. Greitner, "Simulation of tuning forks with a FEA-program for qPlus sensor applications," Bachelor Thesis Universität Regensburg (2012).